Accepted Manuscript

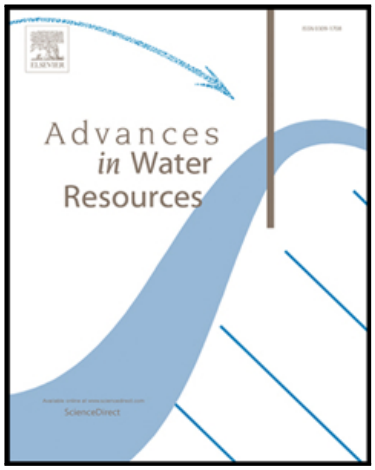

An Extension of Darcy's Law Incorporating Dynamic Length Scales

Yuhang Wang, Saman A. Aryana, Myron B. Allen

PII: S0309-1708(19)30220-9
DOI: https://doi.org/10.1016/j.advwatres.2019.05.010
Reference: ADWR 3337

To appear in: *Advances in Water Resources*

Received date: 11 March 2019
Revised date: 14 May 2019
Accepted date: 16 May 2019

Please cite this article as: Yuhang Wang, Saman A. Aryana, Myron B. Allen, An Extension of Darcy's Law Incorporating Dynamic Length Scales, *Advances in Water Resources* (2019), doi: https://doi.org/10.1016/j.advwatres.2019.05.010

Highlights

- A physics-based macroscale model for multiphase flow in porous media is proposed.
- Immiscible two-phase flow is cast in a vorticity stream-function form.
- A high-resolution simulator resolving all relevant physical scales is developed.
- The proposed model generates evolving fronts that match experimental observations.

An Extension of Darcy's Law Incorporating Dynamic Length Scales

Yuhang Wang[a], Saman A. Aryana[b,c,*], Myron B. Allen[c]

[a] *Department of Petroleum Engineering, University of Wyoming, Laramie, WY 82071, USA*
[b] *Department of Chemical Engineering, University of Wyoming, Laramie, WY 82071, USA*
[c] *Department of Mathematics and Statistics, University of Wyoming, Laramie, WY 82071, USA*

Abstract

We propose a physics-based, macroscale formulation of multiphase porous-media flows that both honors the validity of Darcy's law in steady or near-steady flows and accommodates the effects of heterogeneities and nonlinearities in unsteady flows. The new formulation recognizes that parameters characterizing the system operate at different length-scales. In particular, the use of Darcy's law, predicated on the assumption of near-steady flows, requires dynamic length scales, owing to the possibility of rapid fluctuations in rock properties and fluid saturations attributable to heterogeneity and nonlinearity. We accommodate these dynamic length-scales through dynamic spatial averaging. The length and position of the averaging window are characterized by the length of the mixing zone and the direction of propagation of information in the transport process. We validate the proposed formulation by comparing highly accurate, two-dimensional numerical solutions against core-scale displacement experiments. The proposed paradigm is consistent with the classical multiphase Darcy formulation, in the sense that the latter also represents the results of an averaging approach.

Keywords: Multiphase flow, Nonequilibrium models, High-resolution methods, Flow instability

*Corresponding author
Email address: saryana@uwyo.edu (Saman A. Aryana)

1. Introduction

Accurate mathematical description of multiphase flows in porous media is essential in many practical problems, including groundwater contaminant remediation, geological storage of CO_2, and petroleum reservoir engineering (House et al., 2006; Juanes, 2008; Qiao et al., 2018). Bench- or field-scale simulation of fluid displacement processes in these applications requires macroscale mathematical formulations, which replace the details of flow in the pores with spatially averaged descriptions (Abriola and Pinder, 1985; Bear, 2013; Jiang and Younis, 2015; Wang and Shahvali, 2016; Chabanon et al., 2017). These formulations involve partial differential equations (PDEs) arising from the conservation of mass, momentum and energy (LeVeque, 1992). This paper presents a new formulation of porous-medium flow, based on length-scale averaging, that accommodates effects associated with spatially heterogeneous media and the nonlinearities inherent in multi-fluid flows.

Darcy's law represents the classic macroscale expression of the conservation of momentum for a single fluid phase flowing in a porous solid. It establishes a linear field equation in which the macroscale (Darcy) velocity is proportional to the gradient of a field potential such as the pressure or hydraulic head (Whitaker, 1986). Strictly speaking, Darcy's law is valid for low Reynolds-number, single-fluid, steady flows in which fluid inertia is negligible (Hubbert, 1956; Whitaker, 1986; Dullien, 2012; Neuman, 1977). In some regimes, such as slow flows in nearly homogeneous porous media, it is reasonable to treat the flow as nearly steady, since fluid parcels encounter slowly fluctuating rock properties. However, unless the steady-state velocity field is established, in highly heterogeneous media the hypothesis of nearly steady flow may not be valid, especially at displacement fronts.

Further problems arise in multi-fluid flows. Following Muskat and Meres (1936); Wyckoff and Botset (1936); Leverett (1941), engineers common extend Darcy's law to these flows via the use of nonlinear constitutive relations such as relative permeabilities and capillary pressure. Even though relative per-

meabilities and capillary pressure are often assumed to be local functions of saturation, they also depend on other nonlinear parameters such as saturation history and composition-dependent rock wettability and fluid viscosities (Avraam and Payatakes, 1995; Tang and Kovscek, 2011; Honarpour, 2018). As with heterogeneities, these nonlinear effects can also call into question the assumption of nearly steady flow, since fluids in the mixing zone at a displacement front may encounter rapidly fluctuating rock properties and fluid saturations. In short, since Darcy's law is predicated on the assumption of steady flows, its straightforward application in highly heterogeneous media and in the presence of nonlinearities neglects the variable length scales over which rock properties and fluid saturations vary.

The new formulation presented in this paper addresses this difficulty, accommodating dynamic length scales through dynamic spatial averaging. The length and position of the averaging window are driven by the mixing-zone length and the direction of propagation of information in the transport process. The resulting nonlocal model is consistent in spirit with the classical multiphase Darcy formulation, in the sense that the latter also represents the results of an averaging approach.

In the remainder of the paper, we review previous work, then develop the new model. We focus on flow regimes where flow is appropriately described using DarcyâĂŹs law, or its extension to multi-fluid flow. In that context, the viscous forces are significant compared to the capillary forces. We then validate the proposed formulation by comparing highly accurate, two-dimensional numerical solutions against core-scale displacement experiments. We close with a discussion of the results and some conclusions.

2. Previous Work

In multi-fluid flows, the assumption that constitutive relations depend solely on saturation at a point effectively collapses the functional dependencies along other dimensions, such as saturation history. Even under conditions where

constitutive relations may reasonably be expressed as functions only of local saturation, numerical solutions using high-accuracy numerical methods and precisely measured constitutive relations still fail to model experimental observations (Riaz et al., 2007; Wang et al., 2018).

These results are not surprising. In their classical and most prevalent form, constitutive relations rest on the pivotal assumption of instantaneous local equilibrium and are expressed as functions solely of local saturation (Barenblatt et al., 1997; Ren et al., 2017). This assumption may violate the steady-state requirement that the flow minimizes the dissipation of energy across the medium (King et al., 1995). Compounding this difficulty is the fact that relative permeabilities and capillary pressure are measured based on the assumption of steady-state/equilibrium conditions, then used to describe dynamic processes. The steady-state assumption may adequately approximate systems in which the characteristic time scale of the flow process is large compared to the time it takes for the system to accommodate a perturbation in flow conditions. But there are many cases of interest—such as CO_2 injection into geologic formations—where this assumption fails to reflect the physics (Aryana and Kovscek, 2012). The resulting inaccuracy sharply reduces the predictive capability of the classical Darcy-Muskat model (Muskat and Meres, 1936) for unstable multiphase flow processes (Riaz et al., 2007; Barenblatt et al., 2003).

Several investigators have proposed nonequilibrium models to address this deficiency. Hassanizadeh and Gray (1993b,a) (H&G) proposed a dynamic capillary pressure-saturation relationship motivated by volume averaging of microscopic flow equations and thermodynamic considerations. In this model, the dynamic capillary pressure differs from the static capillary pressure by the product of a dynamic coefficient (τ) and the local rate of change of saturation (Hassanizadeh et al., 2002). The H&G model does not incorporate nonequilibrium effects in the relative permeabilities (Juanes, 2008). A nonequilibrium model proposed by Barenblatt (1971); Barenblatt and Gilman (1987) (BNE) rests on the argument that wetting and non-wetting phases, flowing simultaneously, establish separate networks of flow pathways that connect the flowing

portion of each phase. Any change in capillary pressure causes a reconfiguration of flow pathways (Barenblatt et al., 2003). This reconfiguration changes the connectivity of the flowing phases and the overall hydraulic conductance. The characteristic time required for the flow field to transition from one steady-state arrangement of pathways to another is the redistribution (or relaxation) time, τ. By evaluating the constitutive parameters at time $(t + \tau)$, after relaxation, the BNE model addresses nonequilibrium effects in both relative permeability and capillary pressure. It also effectively relies on a future solution.

Other alternative constitutive models include the extension of capillary pressure to dynamic conditions by Kalaydjian (1987) and dynamic capillary pressure relations that depend on specific interfacial areas and Euler characteristic (Joekar-Niasar et al., 2010; McClure et al., 2018; Niessner and Hassanizadeh, 2008).

Aryana and Kovscek (2013) (A&K) presented a general nonequilibrium formulation that incorporates temporal averages by replacing the local saturation with an integral over the transient (redistribution) time-window. To implement a model of this type, one must solve for a series of future solutions simultaneously, which is not practical. The BNE model circumvents this difficulty, effectively replacing the time integral by a low-order numerical quadrature using the local future solution at the end of the window of integration in place of the time-integral.

The H&G and BNE models lend insight into the implications of unsteady flows. The implementation of these models in large-scale numerical simulators, however, suffers from two important drawbacks. First, redistribution time cannot be directly extracted from experiments for most flow conditions. As a result, it often becomes a fitting parameter in practice (Barenblatt et al., 2003; Ren et al., 2017). Second, the inclusion of these models results in fully nonlinear PDEs whose numerical stability and convergence are sensitive to the numerical value of τ and its magnitude relative to the time step size (Hassanizadeh et al., 2002). As a consequence of the difficulties, large-scale commercial simulators and most research-grade simulators rely on the classical formulation of the

constitutive relations and do not attempt to account for nonequilibrium effects.

3. Proposed Model

The model advanced in this paper rests on two observations. First, time and space are related via the transport equation. Second, Darcy's law is an expression for steady-state flow, and fluid mobility and constitutive relations are established experimentally based on equilibrium or steady-state conditions (Honarpour, 2018). This is true regardless of the experimental method used to measure the constitutive functions: the method can be unsteady, but the estimation is still based on the aforementioned assumptions. In practice, however, macroscale models are used to simulate unsteady and dynamic conditions. Therefore, we should expect to upscale local saturation information to a length scale at which the assumption of near-steady flow is valid—a scale that can be extracted from observations of stable or unstable flows directly and is not a fitting parameter.

3.1. Motivation

To motivate the second observation, recall that a Representative Elementary Volume (REV) is a finite spatial volume whose diameter is the smallest characteristic scale at which variables such as the porosity are well defined (Panfilov, 2013). Strictly speaking, the linear relation between velocity and the gradient field expressed by Darcy's law is valid only under steady-state conditions (Irmay, 1958). As a result, classical macroscale formulations hinge on the fundamental assumption of local phase equilibrium (Barenblatt et al., 2003) and steady flow.

In the multiphase extension of Darcy's law, constitutive functions are assumed to be functions of fluid-phase saturations, not on the specific fluid configurations at the sub-REV scale. For this assumption to be valid, either the fluid configurations in the pores must relax instantaneously to their steady-state configurations or we must average the saturations over a length scale at which the details of transient sub-REV fluid configurations are negligible. To describe

unsteady flow processes, therefore, requires a constitutive-relation averaging-length that may vary in size and may differ from the averaging length used for such properties as the porosity. We refer to the former as the dynamic averaging length, and the latter as the static averaging length. The common practice of treating constitutive relations as functions of local saturation thus implicitly assumes that the static and dynamic averaging lengths are the same. We hypothesize that this assumption is a source of disagreement between numerical solutions and experimental observations. For unsteady flows, the effective values of the saturation-dependent constitutive functions, which define the flux for a given state of saturation, can differ significantly from their values obtained from standard measurements (Barenblatt et al., 2003).

3.2. Formulation

We propose a multiscale view, in which saturation-dependent constitutive relations must be averaged over dynamic averaging lengths. At each point $\boldsymbol{x}$ in space and time t, we define the effective saturation as the weighted average of saturation along the unique particle path passing through the point, over an interval of length l, centered about the given point. The parameter l is the dynamic averaging length; it is a measure of the length of the mixing zone, and may be calculated from observations of the mixing zone at a given time t. As shown in the sketch in Fig. 1, $S_{i,\mathrm{shock}}$ and $S_{i,\mathrm{ahead}}$ represent invading phase saturation values at the shock and ahead of the front (the theoretical displacement front), respectively. $S_{i,\mathrm{shock}}$ is obtained from the solution of the Buckley-Leverett equation (Buckley and Leverett, 1942). We calculate l as the distance between the locus of the theoretical saturation shock, $S_{i,\mathrm{shock}}$, as predicted by the Buckley-Leverett equation (Buckley and Leverett, 1942) and the locus of the actual toe of the invading front, $S_{i,\mathrm{ahead}}$, from the corresponding experimental observations. This procedure approximates the length of the mixing zone while conserving mass that is diffused in the physical observations around the location of the sharp front predicted by the Buckley-Leverett equation.

A critical question for the proposed model is how to determine the length

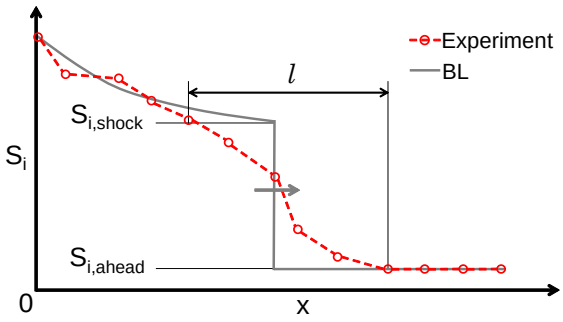

Figure 1: Schematic of evaluation of unstable spreading front.

of the mixing zone, which is driven by the interaction between nonlinearity in the flow equations and geologic heterogeneity (Furtado and Pereira, 2003). The length of the mixing zone does not serve as a tuning parameter; instead we must obtain it through observations. Recent advances in reservoir monitoring methods, e.g., 4D time-lapse seismic monitoring and seismoelectric coupling, facilitate the surveillance of evolution of saturation profiles (Revil et al., 2013; Djuraev et al., 2017; Watanabe et al., 2017), based on which the dynamic length of the mixing zone may be estimated. In addition, numerical investigations (Furtado and Pereira, 2003; Borges et al., 2008a) and experimental observations (Aryana and Kovscek, 2012) suggest that fluid mixing of two-phase immiscible flows in porous media exhibits scaling behavior that can be extracted from observations of the flow. knowledge of this scaling behavior may reduce the number of observations needed for accurate estimates of the dynamic mixing-zone length. The main point is that realistic simulation of multiphase displacement requires realistic estimates of the mixing-zone length, and methods exist to obtain them.

The weighted averaging must respect the direction of flow. In many applications, the time-dependent PDEs governing multiphase flow in porous media are either hyperbolic or nearly so, in the sense that dissipation due to capillarity exerts a small smoothing influence on otherwise sharp fronts. The equations propagate information from upstream to downstream. In the weighted averaging, we assign weights of zero to points in the averaging interval that are

downstream. In the upstream direction, points that are closer to the center of the interval are expected to influence the constitutive relation for the point of interest more heavily. Therefore, points in the upstream direction have weights that decrease with distance from the center of the interval.

We begin with a parametrization $(\boldsymbol{x}(\sigma), t)$ of a typical particle path, using arc length as the parameter σ. The saturation S of a fluid along this path is $S(\boldsymbol{x}(\sigma), t)$, which at a fixed time we abbreviate as $S(\sigma)$. At the point on the particle path where $\sigma = \zeta$, we calculate the corresponding effective saturation $\eta(\zeta)$ as a weighted average of upwind saturation values that lie (1) along the particle path passing through $\boldsymbol{x}(\zeta)$ at time $t(\zeta)$, and (2) within an arc length of $l/2$ along the particle path:

$$\eta(\zeta) = \int_{\zeta - l/2}^{\zeta} w(\sigma) S(\sigma)\, d\sigma. \tag{3.1}$$

Here, l is the width of mixing zone at t, and

$$w(\sigma) = \frac{4}{l}\left[1 + \frac{2}{l}(\sigma - \zeta)\right], \quad \zeta - \frac{l}{2} \le \sigma \le \zeta$$

is the weighting function. With this choice, the weighting function integrates to 1, i.e., $\int w(\sigma)\, d\sigma = 1$, and decreases linearly from the current point ζ along the particle path to a point at distance $l/2$ upstream.

The choice of the linear weighting function is motivated by the expectation that information farther in the upstream direction from a given point will have less impact on the state of flow at that point. Moreover, we choose a linear weighting function in the absence of information that may guide us to a more complex formulation, which may require additional, effectively tuning, parameters. Unlike the H&G and BNE models, which may require the use of iterative methods to solve at each time-step, the proposed averaging approach results in quasi-linear equations, which lend themselves to explicit time-stepping schemes. Moreover, the proposed upstream weighted averaging is performed along the particle path at each point, and the associated computational cost does not increase in higher dimensions, e.g., in two versus three dimensions.

Given the velocity field, we calculate values of the effective saturation η and

evaluate the saturation-dependent constitutive relations at η. To check that the proposed approach is consistent with the classical approach, consider the limiting case in which saturation values relax to steady-state values instantaneously. In this limiting case, the dynamic averaging length vanishes, and we recover the classical formulation. In this case, the effective and actual saturation values are the same.

An important consideration in the development of the mathematical model is availability of appropriate numerical schemes. The classical constitutive relations of multiphase flow in porous media lead to quasi-linear PDEs. Mathematical theory is well-established for scalar quasi-linear PDEs. The inclusion of prominent non-equilibrium models in the constitutive relations, e.g., BNE and H&G models, leads to more challenging, fully nonlinear PDEs where nonlinearities depend not only on the solution but also on the derivative of the solution (Bocharov et al., 1989; Van Duijn et al., 2007). The proposed non-equilibrium model leads to quasi-linear PDEs for which mathematical theory is well developed, especially for scalar quasi-linear PDEs. For instance, in the context of the Buckley-Leverett equation (Buckley and Leverett, 1942), Fourier stability analysis (Anderson and Wendt, 1995; Isaacson and Keller, 2012; Smith, 1985) reveals that the proposed model leads to conditionally stable explicit time-stepping schemes.

4. Numerical Simulation

4.1. Problem Set-up

We tested this formulation using two-dimensional numerical simulations of two-phase fluid displacements on a rectangle having width W and length L. The invading phase, with viscosity μ_i, is injected into the porous medium at the left boundary ($x = 0$) with a constant velocity $\boldsymbol{u}(0, y, t) = (U, 0)$, $U > 0$, displacing the resident phase with viscosity μ_r. We assume that the invading phase pressure is constant at the outlet ($x = L$). The no-flow boundary condition $\boldsymbol{u} \cdot \boldsymbol{n} = 0$ is imposed at the bottom and top boundaries ($y = 0$ and $y = W$),

where $\boldsymbol{n}$ is the unit vector normal to the boundaries. For simplicity we assume incompressible and isothermal conditions. The porous medium is homogeneous with a constant permeability, k, and porosity, ϕ.

The governing equations are

$$\begin{cases} \nabla^2\tilde{\psi} = k\lambda_T(\xi)\left[\nabla\left(\dfrac{1}{k\lambda_T(\xi)}\right)\times\boldsymbol{u}\right]\cdot\hat{\boldsymbol{k}}, \\ \boldsymbol{u} = (u_x, u_y) = (\partial_y\tilde{\psi} + u_x^0, -\partial_x\tilde{\psi}), \\ \phi\,\partial_t S_i + \nabla\cdot[\boldsymbol{u}f_i(\xi)] = -\nabla\cdot[kf_i(\xi)\lambda_r(\xi)\nabla P_c(\xi)] + q_i. \end{cases} \tag{4.1}$$

Here $\tilde{\psi}$ is the fluctuating component of the stream function, ψ, $\hat{\boldsymbol{k}}$ is the unit vector in the positive z-direction, u_x and u_y are scalar components of $\boldsymbol{u}$ along x- and y- axes, respectively. Subscripts i and r denote the invading and the resident phases, respectively. We use ξ to denote either their actual or effective saturation values, depending on the numerical experiment being conducted. The total mobility is $\lambda_T(\xi) = \lambda_i(\xi) + \lambda_r(\xi)$. $P_c(\xi)$ is the capillary pressure; $\boldsymbol{u}$ is the total velocity; and q_i is the volumetric flow rate of the invading phase. The derivation of system (4.1) is referred to Wang et al. (2018). Due to the use of a vorticity stream-function formulation (Tryggvason and Aref, 1983; Meiburg and Homsy, 1988; Tan and Homsy, 1988; Rogerson and Meiburg, 1993), phase pressure does not serve as a simulation variable. The classical model (referred to as CLA) assumes $\xi = S_i$, and the proposed spatial averaging model (referred to as SA) assumes $\xi = \eta_i$.

4.2. Numerical Scheme

4.2.1. Computation of Effective Saturation

The relation between the effective saturation, η, and the actual saturation, S, which passes through the point $\sigma = \zeta$, is given by Eq. (3.1). In a Cartesian coordinate system, the upwind cell of a given cell is determined based on the direction of flow velocity of the given cell. The discrete form of Eq. (3.1) is given by

$$\eta = \sum_{k=0}^{m} W(\sigma_k)S(\sigma_k), \tag{4.2}$$

where σ_k denotes a value of arc length σ assigned to each cell in the computational grid through which the particle path passes, $W(\sigma_k) = \int_{\sigma_{k+1}}^{\sigma_k} w(\sigma)\, d\sigma$. k is the index of upwind cells associated with the target cell. $k = 0$ refers to the target cell itself. m is the maximum number of upwind cells along the particle path such that $\zeta - \sigma_m \leq \frac{l}{2}$, and $\zeta - \sigma_{m+1} > \frac{l}{2}$ are satisfied, or cell $(m+1)$ is located out of the discrete domain. As shown in the sketch in Fig. 2, cells filled in gray denote upwind cells of the target cell filled in black. σ_k is approximated given by

$$\sigma_k \approx \begin{cases} \zeta, & k = 0, \\ \zeta - \sum_{j=1}^{k} d(j-1, j), & k \geq 1, \end{cases} \tag{4.3}$$

where $d(j-1, j)$ is the distance between the center of neighboring cells $(j-1)$ and (j).

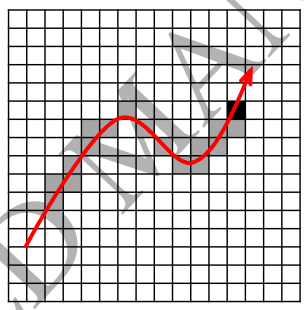

Figure 2: Schematic of upwind cells along a particle path.

4.2.2. Discretization of Governing Equations

To calculate velocity components, u_x and u_y, we apply the Fourier transform to the first equation in system (4.1), resulting in

$$\mathcal{F}\left(\tilde{\psi}\right) = -\frac{\mathcal{F}\left(k\lambda_T(\xi)\left(\nabla\left(\frac{1}{k\lambda_T(\xi)}\right) \times \boldsymbol{u}\right) \cdot \hat{\boldsymbol{k}}\right)}{\left(k_x^2 + k_y^2\right)}, \tag{4.4}$$

where $\mathcal{F}(\cdot)$ denotes the Fourier transform operator, and k_x and k_y are wave numbers along the x- and y- axes, respectively. The spatial derivative term,

$\nabla\left(\frac{1}{k\lambda_T(\xi)}\right)$, is computed with sixth-order compact finite differences (Lele, 1992). The first-order spatial derivatives of $\mathcal{F}\left(\tilde{\psi}\right)$ are given by (Kutz, 2013)

$$\mathcal{F}\left(\partial_x\tilde{\psi}\right) = ik_x\mathcal{F}\left(\tilde{\psi}\right) \text{ and } \mathcal{F}\left(\partial_y\tilde{\psi}\right) = ik_y\mathcal{F}\left(\tilde{\psi}\right), \tag{4.5}$$

where $i^2 = -1$. The spatial derivatives $\partial_x\tilde{\psi}$ and $\partial_y\tilde{\psi}$ of the fluctuating component of the stream function are computed by performing an inverse-transform on both sides of Eq. (4.5).

The numerical scheme for the transport equation in system (4.1) is obtained from integration of that equation over cell $V_{j,\ell}$:

$$\int_{V_{j,\ell}} \phi\partial_t S_i \, dA + \int_{\partial V_{j,\ell}} f_i(\xi)\boldsymbol{u}\cdot\boldsymbol{n}\, ds = -\int_{\partial V_{j,\ell}} kf_i(\xi)\lambda_r(\xi)\nabla P_c(\xi)\cdot\boldsymbol{n}\, ds, \tag{4.6}$$

where the external invading phase volumetric flow rate is assumed to be zero ($q_i = 0$). $V_{j,l}$ is assumed to be rectangular with area of $\Delta x\Delta y$.

The spatial derivative of the dissipation flux is computed using fourth-order central differences. To reduce numerical dispersion arising from the discretization of the convection flux and to capture saturation fronts without introducing misleading oscillations, a high-order, Total Variation Diminishing (TVD) scheme (Harten, 1983; Sweby, 1984) is applied to the convection flux. This work implements the central-upwind scheme (Kurganov and Levy, 2000; Kurganov and Tadmor, 2000; Kurganov et al., 2001), where the intermediate values are constructed using the fifth-order Weighted Essentially Nonoscillatory (WENO) scheme (Jiang and Shu, 1996; Shu, 2009). Details of the discretization of convection flux are presented in Appendix A. The third-order TVD Runge–Kutta method (Gottlieb and Shu, 1998; Gottlieb et al., 2001) is used for the temporal discretization. The transport equation in system (4.1) is rewritten as

$$\frac{\mathrm{d}S_i}{\mathrm{d}t} \approx L(\xi, \boldsymbol{u}), \tag{4.7}$$

where $L(\xi,\boldsymbol{u}) = \frac{1}{\phi\Delta x\Delta y}\left(C(\xi,\boldsymbol{u}) + D(\xi)\right)$, $C(\xi,\boldsymbol{u})$ and $D(\xi)$ are approximations to the discretization of convection and dissipation fluxes, respectively.

The time marching scheme over (t_n, t_{n+1}) is given by

$$\begin{aligned} S_i^{(1)} &= S_i^n + \Delta t L\left(S_i^n, \boldsymbol{u}^{n+1}\right), \\ S_i^{(2)} &= \frac{3}{4}S_i^n + \frac{1}{4}S_i^{(1)} + \frac{1}{4}\Delta t L\left(S_i^{(1)}, \boldsymbol{u}^{n+1}\right), \\ S_i^{n+1} &= \frac{1}{3}S_i^n + \frac{2}{3}S_i^{(2)} + \frac{2}{3}\Delta t L\left(S_i^{(2)}, \boldsymbol{u}^{n+1}\right), \end{aligned} \tag{4.8}$$

and

$$\begin{aligned} \eta_i^{(1)} &= S_i^n + \Delta t L\left(\eta_i^n, \boldsymbol{u}^{n+1}\right), \\ \eta_i^{(2)} &= \frac{3}{4}S_i^n + \frac{1}{4}\eta_i^{(1)} + \frac{1}{4}\Delta t L\left(\eta_i^{(1)}, \boldsymbol{u}^{n+1}\right), \\ S_i^{n+1} &= \frac{1}{3}S_i^n + \frac{2}{3}\eta_i^{(2)} + \frac{2}{3}\Delta t L\left(\eta_i^{(2)}, \boldsymbol{u}^{n+1}\right), \end{aligned} \tag{4.9}$$

for the CLA and SA models, respectively. The superscript n and $n+1$ denote time step counters. Δt is time step size.

4.3. Experimental Data & Simulation Input

Physical observations used in this study are based on a series of core-scale displacement experiments. The centerpiece of the drainage experiments is a strongly water-wet, cylindrical Berea sandstone cores 5.08 cm in diameter and 60 cm in length. The imbibition experiments are conducted using a strongly water-wet, cylindrical Berea sandstone cores 5.1 cm in diameter and 52 cm in length. The cores are characterized as homogeneous porous media with negligible variations in porosity and permeability along the main direction of flow. At the initial stage, cores are saturated with the resident phase uniformly. X-ray tomography is used to collect in-situ saturation distribution data nondestructively (Tang and Kovscek, 2011; Aryana and Kovscek, 2012). Simulation parameters representative of the experiments are used in numerical simulation models. Data shown in Table 1 represent core-scale imbibition and drainage displacement experiments using pairs of immiscible fluids. The viscosity ratio in Table 1 is the ratio of the viscosity of resident fluid to that of the invading fluid. Endpoint and total shock mobility ratios are often used as indicators of the onset of flow instability (Hagoort, 1974; Yortsos and Hickernell, 1989; Riaz and Tchelepi, 2004; Beliveau, 2009; Berg and Ott, 2012), where mobility ratios larger than unity indicate an unstable displacement.

Corresponding simulation parameters are presented in Table 2. Imbibition relative permeability functions are based on steady-state measurements (Tang and Kovscek, 2011), and for drainage, Corey-type relative permeability functions (Corey, 1954) are used where the end-points and exponents are guided by steady-state displacement experiments (Aryana and Kovscek, 2013). We use capillary pressure data obtained from a mercury intrusion experiment (Ren et al., 2017). Random perturbations are introduced in the initial condition (Ruith and Meiburg, 2000; Riaz and Tchelepi, 2006). We choose the spatial mesh size to be no greater than the critical wavelength resulting from a linear stability analysis to resolve all relevant physical scales (Chuoke et al., 1959; Hagoort, 1974; Saffman and Taylor, 1988; Feder, 2013). For each case, we plot one-dimensional profiles of saturation versus dimensionless distance x_D, obtained by averaging the saturation along cross-sectional lines perpendicular to the x-direction at three different times. Dimensionless dynamic averaging lengths, l_D, and the associated dimensionless simulation times, t_D, which represent injected pore volumes, are tabulated in Table 3.

Exp #	Type	Viscosity Ratio	Mobility Ratio	
			end point	total shock
1	Imbibition	27.6	2.07	0.82
2	Imbibition	155.3	11.63	2.29
3	Drainage	2.1	5.88	0.96
4	Drainage	15.0	42.00	1.78

Table 1: Experimental data used in this study.

5. Results and Discussions

Figs. 3 and 4 show saturation maps obtained from two-dimensional numerical solutions, and their equivalent one-dimensional saturation profiles obtained by cross-sectional averaging, along with experimental data are presented in Figs.

Type	Length	Porosity	Absolute Permeability	Injection Velocity
	m	-	m^2	m/s
Imbibition	0.52	0.20	0.377e-12	4.051e-6
Drainage	0.60	0.19	0.254e-12	4.051e-6

Table 2: Physical parameters used in numerical simulations.

5 and 6. These results demonstrate the efficacy of the proposed model in capturing physical observations. The agreement between the proposed model and physical observations is especially pronounced when compared to solutions of the classical formulation.

We compare experimental data and numerical solutions for two cases: stable displacements, in which the invading fluid displaces the resident fluid in a piston-like fashion, and unstable displacements, in which the invading fluid forms viscous fingers as it moves downstream. Endpoint mobility ratio appears to be an appropriate criterion for the onset of instabilities in the experiments, whereas total shock mobility ratio is a better indicator of the onset of flow instabilities in the simulation results. Saturation maps presented in Figs. 3 and 4 show that for the fluid systems in experiments #1 and #3, fluctuations in the interface decay as displacement progresses, so the displacement is stable. The mixing zone becomes a thin, piston-like band perpendicular to the injection direction. The resulting one-dimensional saturation profiles exhibit relatively sharp fronts. For fluid systems given by experiments #2 and #4, fluctuations grow and develop into prominent viscous fingers. These fingers grow longer with time, indicating unstable displacement. The viscous fingers are reflected as spreading fronts in the cross-sectionally averaged saturation profiles in Figs. 5b and 5d.

First consider the results of the CLA model. As shown in Fig. 5, cross-sectionally averaged saturation profiles obtained from two-dimensional simula-

Exp #		Saturation Profiles		
		i	ii	iii
1	t_D	0.08	0.12	0.18
	l_D	0.23	0.32	0.54
2	t_D	0.02	0.06	0.10
	l_D	0.16	0.23	0.50
3	t_D	0.08	0.13	0.18
	l_D	0.19	0.30	0.39
4	t_D	0.03	0.08	0.14
	l_D	0.32	0.53	0.64

Table 3: Values of dimensionless dynamic lengths, and associated dimensionless times, extracted from experimental observations.

tions using the CLA model fail to capture the dynamics of the displacement fronts observed in experiments. In the cases of stable displacement, as indicated by the total shock mobility ratio, simulation results exhibit relatively sharp fronts, as shown in Figs. 5a and 5c. In cases of unstable displacement, shown in Figs. 5b and 5d, saturation profiles from the CLA model show evolving fronts with increasing length of the mixing zone. In both cases the CLA model exhibits significant deviations from the the experimental data.

Next consider the results of the SA model proposed in this paper. Saturation maps presented in Figs. 3a and 4a show that, for the cases of stable displacement, in comparison with the CLA model, the SA model produces smoother transition zones in the vicinity of the saturation fronts. The highly-resolved viscous fingers that appear in Figs. 3b and 4b are smeared, and variations in the amplitude of fingers are reduced. This smearing is reflected in the cross-sectionally averaged saturation profiles as spreading of the saturation front. This numerical spreading lengthens the mixing zone for all the four experiments. Sat-

uration profiles obtained from the SA model are in remarkable agreement with experimental data, and they appear to capture the evolving nature of instabilities observed in the experiments.

As an additional benefit, the SA model alleviates the numerical instability and convergence issues arising from the BNE and H&G nonequilibrium models. Accordingly, we discretized the proposed model using an explicit time-stepping scheme. The dynamic length-scales in the SA model are extracted directly from experimental observations.

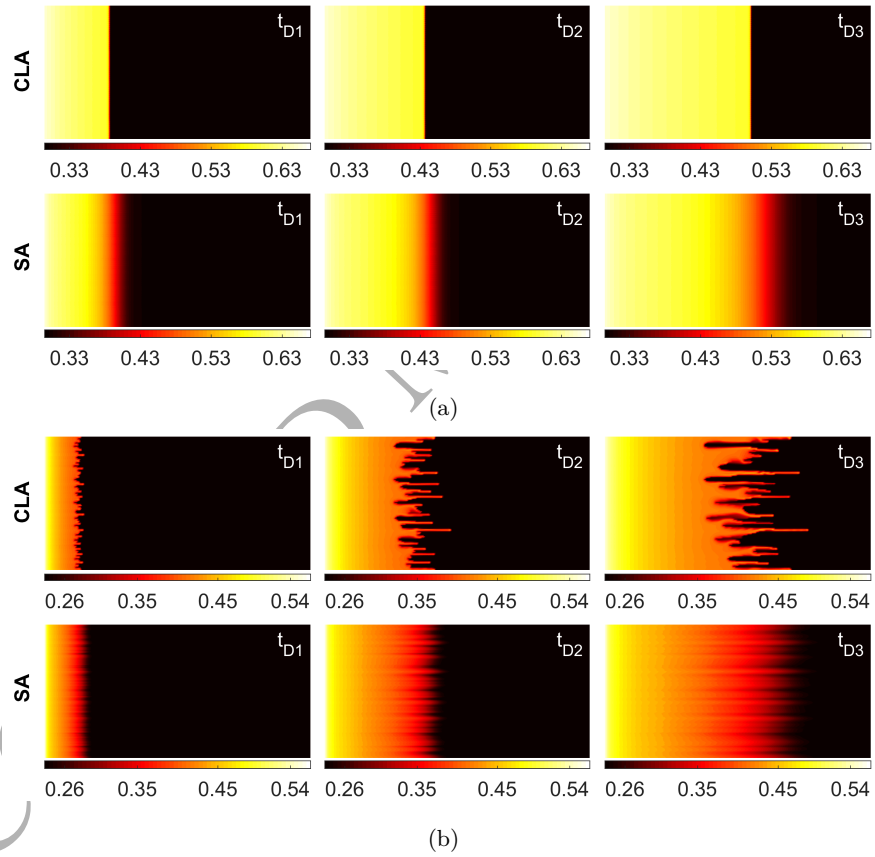

Figure 3: Comparisons of the saturation maps obtained with the CLA and the SA models in imbibition displacements. Fluid systems are given by (a) experiment #1, and (b) experiment #2.

6. Conclusion

This paper proposes a novel, self-consistent, and physics-based mathematical formulation for the relative permeabilities and capillary functions used to model multiphase flow in porous media. We replace the standard dependencies of these constitutive variables on fluid saturation at a point by dependencies on spatial averages along particle paths. The resulting formulation evaluates the variables at saturation values that better reflect the scales over which one can reasonably treat the pore-scale fluid distribution as nearly steady-state. In this respect, the new model honors the steady-state assumption underlying the extension of Darcy's law to multiple phases. The averaging window is dynamic, and its length-scale may be directly obtained from physical observations.

To test the new model, we developed a two-dimensional, high-resolution numerical simulator that resolves all relevant physical scales and elucidates the predictive capabilities of the classical and proposed models across a wide range of parameters and experimental observations. The simulator casts the flow equations in a vorticity-stream-function form. The Fourier transform is used to solve the vorticity-stream-function equation. The advective flux in the transport equation is computed using a central-upwind scheme, where the intermediate values are constructed using the fifth-order WENO scheme. The coupled vorticity-stream-function equation and the transport equation are solved in a sequential manner through explicit time-stepping.

We compare numerical results for homogeneous porous media with core-scale imbibition and drainage experiments in the literature. Saturation maps obtained using the proposed model demonstrate that the averaging of saturations over dynamic length scales has a diffusive effect, which smears of viscous fingers that are otherwise well resolved via the classical model. The proposed model captures reproducible relevant properties of the evolving fronts in the experiments, namely the length of the mixing zone and the position of the leading edge of the front in one-dimensional saturation profiles. The proposed model is consistent with the physics and is predictive in stable and unstable fluid displacements.

Acknowledgments

The corresponding author gratefully acknowledges the Donors of the American Chemical Society Petroleum Research Fund (55795-DNI9) for partial support of this research. The writing stage of this research was supported as part of the Center for Mechanistic Control of Water-Hydrocarbon-Rock Interactions in Unconventional and Tight oil Formations (CMC-UF), an Energy Frontier Research Center funded by the U.S. Department of Energy, Office of Science under DOE (BES) Award DE-SC0019165. The corresponding author also thanks Prof. Frederico Furtado and Prof. Victor Ginting for our lively discussions.

References

Abriola LM, Pinder GF. A multiphase approach to the modeling of porous media contamination by organic compounds: 1. equation development. Water resources research 1985;21(1):11–8.

Anderson JD, Wendt J. Computational fluid dynamics. volume 206. Springer, 1995.

Aryana SA, Kovscek AR. Experiments and analysis of drainage displacement processes relevant to carbon dioxide injection. Physical Review E 2012;86(6):066310.

Aryana SA, Kovscek AR. Nonequilibrium effects and multiphase flow in porous media. Transport in porous media 2013;97(3):373–94.

Avraam DG, Payatakes AC. Flow regimes and relative permeabilities during steady-state two-phase flow in porous media. Journal of Fluid Mechanics 1995;293:207–36.

Barenblatt GI. Filtration of two nonmixing fluids in a homogeneous porous medium. Fluid Dynamics 1971;6(5):857–64.

Barenblatt GI, Garcia Azorero J, De Pablo A, Vazquez JL. Mathematical model of the non equilibrium water oil displacement in porous strata. Applicable Analysis 1997;65(1-2):19–45.

Barenblatt GI, Gilman AA. A mathematical model of non-equilibrium counter-current capillary imbibition. Eng Phys Journal 1987;52(3):46–461.

Barenblatt GI, Patzek TW, Silin DB. The mathematical model of nonequilibrium effects in water-oil displacement. SPE journal 2003;8(04):409–16.

Bear J. Dynamics of fluids in porous media. Courier Corporation, 2013.

Beliveau D. Waterflooding viscous oil reservoirs. SPE Reservoir Evaluation & Engineering 2009;12(05):689–701.

Berg S, Ott H. Stability of CO_2–brine immiscible displacement. International Journal of Greenhouse Gas Control 2012;11:188–203.

Bocharov O, Kuznetsov V, Chekhovich YV. Numerical study of the nonequilibrium filtration of immiscible liquids. Journal of Engineering Physics and Thermophysics 1989;57(1):803–6.

Borges M, Furtado F, Pereira F, Souto HA. Scaling analysis for the tracer flow problem in self-similar permeability fields. Multiscale Modeling & Simulation 2008a;7(3):1130–47.

Borges R, Carmona M, Costa B, Don WS. An improved weighted essentially non-oscillatory scheme for hyperbolic conservation laws. Journal of Computational Physics 2008b;227(6):3191–211.

Buckley SE, Leverett M. Mechanism of fluid displacement in sands. Transactions of the AIME 1942;146(01):107–16.

Chabanon M, Valdés-Parada FJ, Ochoa-Tapia JA, Goyeau B. Large-scale model of flow in heterogeneous and hierarchical porous media. Advances in Water Resources 2017;109:41–57.

Chuoke R, Van Meurs P, van der Poel C. The instability of slow, immiscible, viscous liquid-liquid displacements in permeable media. Petroluem Transactions, AIME 1959;216:188–94.

Corey AT. The interrelation between gas and oil relative permeabilities. Producers monthly 1954;19(1):38–41.

Djuraev U, Jufar SR, Vasant P. A review on conceptual and practical oil and gas reservoir monitoring methods. Journal of Petroleum Science and Engineering 2017;152:586–601.

Dullien FAL. Porous media: fluid transport and pore structure. Academic press, 2012.

Feder J. Fractals. Springer Science & Business Media, 2013.

Furtado F, Pereira F. Crossover from nonlinearity controlled to heterogeneity controlled mixing in two-phase porous media flows. Computational Geosciences 2003;7(2):115–35.

Gottlieb S, Shu CW. Total variation diminishing Runge-Kutta schemes. Mathematics of computation of the American Mathematical Society 1998;67(221):73–85.

Gottlieb S, Shu CW, Tadmor E. Strong stability-preserving high-order time discretization methods. SIAM review 2001;43(1):89–112.

Hagoort J. Displacement stability of water drives in water-wet connate-water-bearing reservoirs. Society of Petroleum Engineers Journal 1974;14(01):63–74.

Harten A. High resolution schemes for hyperbolic conservation laws. Journal of computational physics 1983;49(3):357–93.

Hassanizadeh SM, Celia MA, Dahle HK. Dynamic effect in the capillary pressure–saturation relationship and its impacts on unsaturated flow. Vadose Zone Journal 2002;1(1):38–57.

Hassanizadeh SM, Gray WG. Thermodynamic basis of capillary pressure in porous media. Water resources research 1993a;29(10):3389–405.

Hassanizadeh SM, Gray WG. Toward an improved description of the physics of two-phase flow. Advances in Water Resources 1993b;16(1):53–67.

Honarpour MM. Relative permeability of petroleum reservoirs. CRC press, 2018.

House KZ, Schrag DP, Harvey CF, Lackner KS. Permanent carbon dioxide storage in deep-sea sediments. Proceedings of the National Academy of Sciences 2006;103(33):12291–5.

Hubbert MK. Darcy's law and the field equations of the flow of underground fluids. Transactions of the American Institute of Mining and Metallurgical Engineers 1956;207:222–39.

Irmay S. On the theoretical derivation of Darcy and Forchheimer formulas. Eos, Transactions American Geophysical Union 1958;39(4):702–7.

Isaacson E, Keller HB. Analysis of numerical methods. Courier Corporation, 2012.

Jiang GS, Shu CW. Efficient implementation of weighted ENO schemes. Journal of computational physics 1996;126(1):202–28.

Jiang J, Younis RM. A multimechanistic multicontinuum model for simulating shale gas reservoir with complex fractured system. Fuel 2015;161:333–44.

Joekar-Niasar V, Hassanizadeh SM, Dahle HK. Non-equilibrium effects in capillarity and interfacial area in two-phase flow: dynamic pore-network modelling. Journal of Fluid Mechanics 2010;655:38–71.

Juanes R. Nonequilibrium effects in models of three-phase flow in porous media. Advances in Water Resources 2008;31(4):661–73.

Kalaydjian F. A macroscopic description of multiphase flow in porous media involving spacetime evolution of fluid/fluid interface. Transport in Porous Media 1987;2(6):537–52.

King M, King P, McGill C, Williams J. Effective properties for flow calculations. Transport in Porous Media 1995;20(1-2):169–96.

Kurganov A, Levy D. A third-order semidiscrete central scheme for conservation laws and convection-diffusion equations. SIAM Journal on Scientific Computing 2000;22(4):1461–88.

Kurganov A, Noelle S, Petrova G. Semidiscrete central-upwind schemes for hyperbolic conservation laws and Hamilton–Jacobi equations. SIAM Journal on Scientific Computing 2001;23(3):707–40.

Kurganov A, Petrova G, Popov B. Adaptive semidiscrete central-upwind schemes for nonconvex hyperbolic conservation laws. SIAM Journal on Scientific Computing 2007;29(6):2381–401.

Kurganov A, Tadmor E. New high-resolution central schemes for nonlinear conservation laws and convection–diffusion equations. Journal of Computational Physics 2000;160(1):241–82.

Kutz JN. Data-driven modeling & scientific computation: methods for complex systems & big data. Oxford University Press, 2013.

Lele SK. Compact finite difference schemes with spectral-like resolution. Journal of computational physics 1992;103(1):16–42.

LeVeque RJ. Numerical methods for conservation of laws. BirkhÃďuser Basel, 1992.

Leverett MC. Capillary behavior in porous solids. Transactions of the American Institute of Mining and Metallurgical Engineers 1941;142:152–69.

McClure JE, Armstrong RT, Berrill MA, Schlüter S, Berg S, Gray WG, Miller CT. Geometric state function for two-fluid flow in porous media. Physical Review Fluids 2018;3(8):084306.

Meiburg E, Homsy GM. Nonlinear unstable viscous fingers in Hele-Shaw flows. II. numerical simulation. The Physics of fluids 1988;31(3):429–39.

Muskat M, Meres MW. The flow of heterogeneous fluids through porous media. Physics 1936;7(9):346–63.

Neuman SP. Theoretical derivation of Darcy's law. Acta Mechanica 1977;25(3-4):153–70.

Niessner J, Hassanizadeh SM. A model for two-phase flow in porous media including fluid-fluid interfacial area. Water Resources Research 2008;44(8).

Panfilov M. Macroscale models of flow through highly heterogeneous porous media. volume 16. Springer Science & Business Media, 2013.

Qiao Y, Andersen P, Evje S, Standnes D. A mixture theory approach to model co-and counter-current two-phase flow in porous media accounting for viscous coupling. Advances in Water Resources 2018;112:170–88.

Ren G, Rafiee J, Aryana SA, Younis RM. A bayesian model selection analysis of equilibrium and nonequilibrium models for multiphase flow in porous media. International Journal of Multiphase Flow 2017;89:313–20.

Revil A, Barnier G, Karaoulis M, Sava P, Jardani A, Kulessa B. Seismoelectric coupling in unsaturated porous media: theory, petrophysics, and saturation front localization using an electroacoustic approach. Geophysical Journal International 2013;196(2):867–84.

Riaz A, Tang GQ, Tchelepi HA, Kovscek AR. Forced imbibition in natural porous media: Comparison between experiments and continuum models. Physical Review E 2007;75(3):036305.

Riaz A, Tchelepi HA. Linear stability analysis of immiscible two-phase flow in porous media with capillary dispersion and density variation. Physics of Fluids 2004;16(12):4727–37.

Riaz A, Tchelepi HA. Numerical simulation of immiscible two-phase flow in porous media. Physics of Fluids 2006;18(1):014104.

Rogerson A, Meiburg E. Numerical simulation of miscible displacement processes in porous media flows under gravity. Physics of Fluids A: Fluid Dynamics 1993;5(11):2644–60.

Ruith M, Meiburg E. Miscible rectilinear displacements with gravity override. part 1. homogeneous porous medium. Journal of Fluid Mechanics 2000;420:225–57.

Saffman PG, Taylor FRSSG. The penetration of a fluid into a porous medium or Hele-Shaw cell containing a more viscous liquid. In: Dynamics of Curved Fronts. Elsevier; 1988. p. 155–74.

Shi J, Hu C, Shu CW. A technique of treating negative weights in WENO schemes. Journal of Computational Physics 2002;175(1):108–27.

Shu CW. High order weighted essentially nonoscillatory schemes for convection dominated problems. SIAM review 2009;51(1):82–126.

Smith GD. Numerical solution of partial differential equations: finite difference methods. Oxford university press, 1985.

Sweby PK. High resolution schemes using flux limiters for hyperbolic conservation laws. SIAM journal on numerical analysis 1984;21(5):995–1011.

Tan CT, Homsy GM. Simulation of nonlinear viscous fingering in miscible displacement. The Physics of fluids 1988;31(6):1330–8.

Tang GQ, Kovscek AR. High resolution imaging of unstable, forced imbibition in berea sandstone. Transport in porous media 2011;86(2):617–34.

Tryggvason G, Aref H. Numerical experiments on Hele Shaw flow with a sharp interface. Journal of Fluid Mechanics 1983;136:1–30.

Van Duijn C, Peletier LA, Pop IS. A new class of entropy solutions of the Buckley–Leverett equation. SIAM Journal on Mathematical Analysis 2007;39(2):507–36.

Wang Y, Aryana SA, Furtado F, Ginting V. Analysis of nonequilibrium effects and flow instability in immiscible two-phase flow in porous media. Advances in Water Resources 2018;122:291–303.

Wang Y, Shahvali M. Discrete fracture modeling using Centroidal Voronoi grid for simulation of shale gas plays with coupled nonlinear physics. Fuel 2016;163:65–73.

Watanabe S, Han J, Hetz G, Datta-Gupta A, King MJ, Vasco DW, et al. Streamline-based time-lapse-seismic-data integration incorporating pressure and saturation effects. SPE Journal 2017;22(04):1–261.

Whitaker S. Flow in porous media I: A theoretical derivation of Darcy's law. Transport in porous media 1986;1(1):3–25.

Wyckoff RD, Botset HG. The flow of gas-liquid mixtures through unconsolidated sands. Physics 1936;7(9):325–45.

Yortsos YC, Hickernell FJ. Linear stability of immiscible displacement in porous media. SIAM Journal on Applied Mathematics 1989;49(3):730–48.

Zahran YH. An efficient WENO scheme for solving hyperbolic conservation laws. Applied Mathematics and Computation 2009;212(1):37–50.

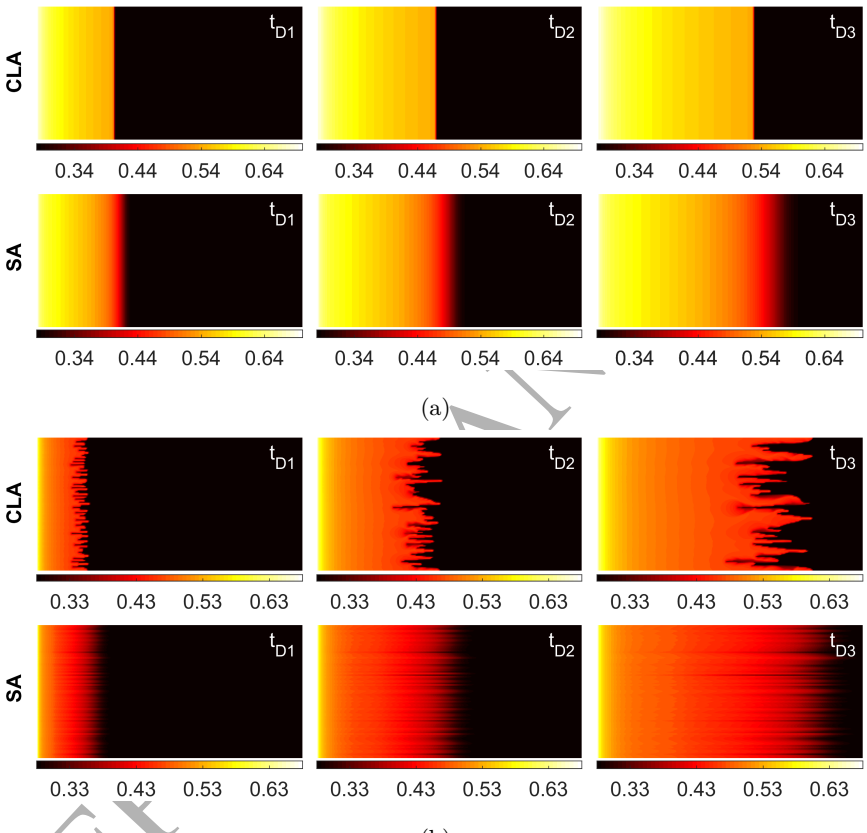

(a)

(b)

Figure 4: Comparisons of the saturation maps obtained with the CLA and the SA models in drainage displacements. Fluid systems are given by (a) experiment #3, and (b) experiment #4.

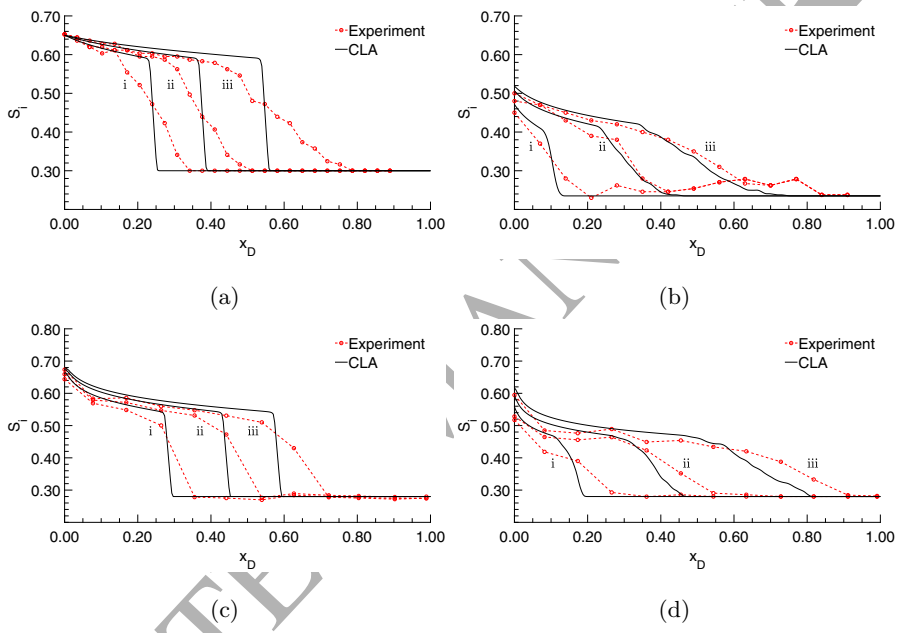

Figure 5: Comparisons of the cross-sectional average of saturation obtained with experiments and the CLA model. Fluid systems are given by (a) experiment #1, (b) experiment #2, (c) experiment #3, and (d) experiment #4.

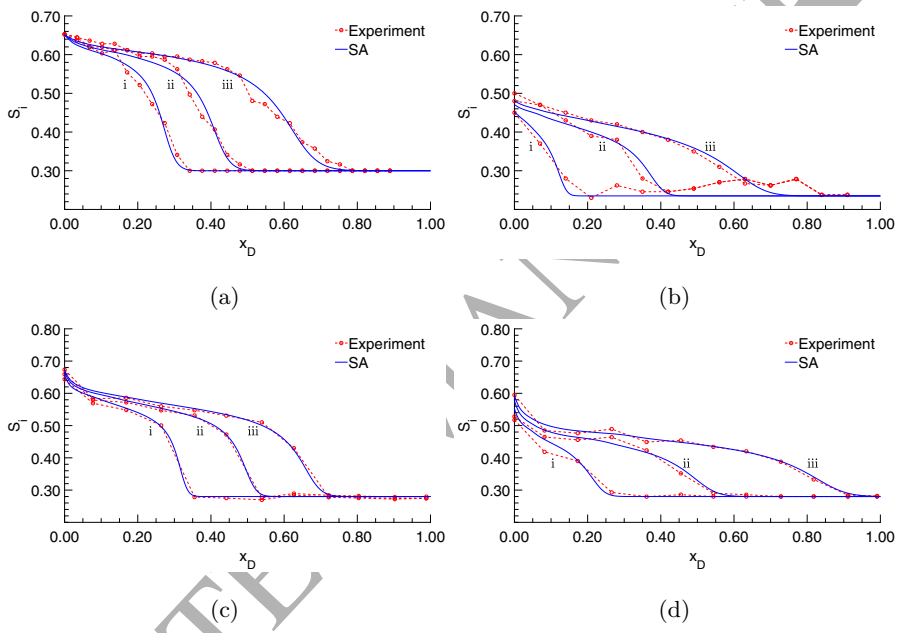

Figure 6: Comparisons of the cross-sectional average of saturation obtained with experiments and the SA model. Fluid systems are given by (a) experiment #1, (b) experiment #2, (c) experiment #3, and (d) experiment #4.

Appendix A. Discretization of the Convection Flux in Transport Equation

The central-upwind scheme (Kurganov and Tadmor, 2000; Kurganov and Levy, 2000; Kurganov et al., 2001) is applied to the convection flux. For brevity, we consider one-dimensional system of cells with uniform spacing. The semi-discrete central-upwind scheme (Kurganov et al., 2001) is given by (The dissipation flux is not included in the description below)

$$\frac{\mathrm{d}}{\mathrm{d}t}\, S_i|_j = -\frac{u_x|_j}{\phi \Delta x}\left(F(\xi_\theta)|_{j+\frac{1}{2}} - F(\xi_\theta)|_{j-\frac{1}{2}} \right), \tag{A.1}$$

where

$$F(\xi_\theta)|_{j+\frac{1}{2}} = \frac{a^+_{j+\frac{1}{2}} f\left(\xi^-_{j+\frac{1}{2}}\right) - a^-_{j+\frac{1}{2}} f\left(\xi^+_{j+\frac{1}{2}}\right)}{a^+_{j+\frac{1}{2}} - a^-_{j+\frac{1}{2}}} + \frac{a^+_{j+\frac{1}{2}} a^-_{j+\frac{1}{2}}}{a^+_{j+\frac{1}{2}} - a^-_{j+\frac{1}{2}}} \left[\xi^+_{j+\frac{1}{2}} - \xi^-_{j+\frac{1}{2}} \right], \tag{A.2}$$

and $f(\xi) = f_i(\xi)$. Subscript i denotes the invading phase. In Eq. (A.2), $\xi^-_{j+\frac{1}{2}}$ and $\xi^+_{j+\frac{1}{2}}$ are left and right intermediate values at cell interface $x_{j+\frac{1}{2}}$. $a^-_{j+\frac{1}{2}}$ and $a^+_{j+\frac{1}{2}}$ are local speeds of propagation at cell interface $x_{j+\frac{1}{2}}$. In this work we take (Kurganov et al., 2001, 2007)

$$a^+_{j+\frac{1}{2}} = -a^-_{j+\frac{1}{2}} = a_{j+\frac{1}{2}}, \tag{A.3}$$

where

$$a_{j+\frac{1}{2}} = \max_{\xi \in \left[\xi^-_{j+\frac{1}{2}}, \xi^+_{j+\frac{1}{2}}\right]} f'(\xi). \tag{A.4}$$

Substituting Eq. (A.3) into Eq. (A.2), the numerical flux reduces to

$$F(\xi_\theta)|_{j+\frac{1}{2}} = \frac{f\left(\xi^+_{j+\frac{1}{2}}\right) + f\left(\xi^-_{j+\frac{1}{2}}\right)}{2} - \frac{a_{j+\frac{1}{2}}}{2}\left[\xi^+_{j+\frac{1}{2}} - \xi^-_{j+\frac{1}{2}} \right]. \tag{A.5}$$

$F(\xi_\theta)|_{j-\frac{1}{2}}$ is obtained in a similar fashion given by

$$F(\xi_\theta)|_{j-\frac{1}{2}} = \frac{f\left(\xi^+_{j-\frac{1}{2}}\right) + f\left(\xi^-_{j-\frac{1}{2}}\right)}{2} - \frac{a_{j-\frac{1}{2}}}{2}\left[\xi^+_{j-\frac{1}{2}} - \xi^-_{j-\frac{1}{2}} \right]. \tag{A.6}$$

Intermediate values, $\xi^-_{j+\frac{1}{2}}$ and $\xi^+_{j+\frac{1}{2}}$, are constructed using the fifth-order Weighted Essentially Nonoscillatory (WENO) scheme (Jiang and Shu, 1996; Shu, 2009).

Reconstructions are based on five-point stencils with one point biased to the left ($\xi^-_{j+\frac{1}{2}}$), and one point biased to the right ($\xi^+_{j+\frac{1}{2}}$), respectively.

$\xi^-_{j+\frac{1}{2}}$ is computed using the stencil $\{I_{i-2}, I_{i-1}, I_i, I_{i+1}, I_{i+2}\}$, given by (Shi et al., 2002; Zahran, 2009)

$$\xi^-_{j+\frac{1}{2}} = \sum_{i=0}^{2} w_i^- \xi^{-,(i)}_{j+\frac{1}{2}}, \tag{A.7}$$

where

$$\begin{aligned}
\xi^{-,(0)}_{j+\frac{1}{2}} &= \frac{1}{6}\left(2\xi_{j-2} - 7\xi_{j-1} + 11\xi_j\right), \\
\xi^{-,(1)}_{j+\frac{1}{2}} &= \frac{1}{6}\left(-\xi_{j-1} + 5\xi_j + 2\xi_{j+1}\right), \\
\xi^{-,(2)}_{j+\frac{1}{2}} &= \frac{1}{6}\left(2\xi_j + 5\xi_{j+1} - \xi_{j+2}\right).
\end{aligned} \tag{A.8}$$

And w_i^- are nonlinear weights given by

$$w_i^- = \frac{\tilde{w}_i^-}{\sum_{k=0}^{2} \tilde{w}_k^-}, \tag{A.9}$$

where

$$\tilde{w}_k^- = \frac{\gamma_k^-}{\tilde{\beta}_k^-}, \tag{A.10}$$

with the linear weights given by $\gamma_0^- = 0.1$, $\gamma_1^- = 0.6$, and $\gamma_2^- = 0.3$. $\tilde{\beta}_k^-$ are the smoothness indicators given by (Borges et al., 2008b)

$$\tilde{\beta}_k^- = \frac{\beta_k^- + \varepsilon}{\beta_k^- + \varepsilon + \tau_5^-}, \tag{A.11}$$

where ε is a parameter used to avoid the division by zero in the denominator. β_k^- is given by (Shi et al., 2002)

$$\begin{aligned}
\beta_0^- &= \frac{13}{12}\left(\xi_{j-2} - 2\xi_{j-1} + \xi_j\right)^2 + \frac{1}{4}\left(\xi_{j-2} - 4\xi_{j-1} + 3\xi_j\right)^2, \\
\beta_1^- &= \frac{13}{12}\left(\xi_{j-1} - 2\xi_j + \xi_{j+1}\right)^2 + \frac{1}{4}\left(\xi_{j-1} - \xi_{j+1}\right)^2, \\
\beta_2^- &= \frac{13}{12}\left(\xi_j - 2\xi_{j+1} + \xi_{j+2}\right)^2 + \frac{1}{4}\left(3\xi_j - 4\xi_{j+1} + \xi_{j+2}\right)^2,
\end{aligned} \tag{A.12}$$

and

$$\tau_5^- = |\beta_0^- - \beta_2^-|. \tag{A.13}$$

$\xi^+_{j+\frac{1}{2}}$ is computed using the stencil $\{I_{i-1}, I_i, I_{i+1}, I_{i+2}, I_{i+3}\}$, given by

$$\xi^+_{j+\frac{1}{2}} = \sum_{i=0}^{2} w_i^+ \xi^{+,(i)}_{j+\frac{1}{2}}, \tag{A.14}$$

where

$$\begin{aligned}
\xi^{+,(0)}_{j+\frac{1}{2}} &= \frac{1}{6}\left(-\xi_{j-1} + 5\xi_j + 2\xi_{j+1}\right), \\
\xi^{+,(1)}_{j+\frac{1}{2}} &= \frac{1}{6}\left(2\xi_j + 5\xi_{j+1} - \xi_{j+2}\right), \\
\xi^{+,(2)}_{j+\frac{1}{2}} &= \frac{1}{6}\left(11\xi_{j+1} - 7\xi_{j+2} - 2\xi_{j+3}\right).
\end{aligned} \tag{A.15}$$

And w_i^+ are nonlinear weights given by

$$w_i^+ = \frac{\tilde{w}_i^+}{\sum_{k=0}^{2} \tilde{w}_k^+}, \tag{A.16}$$

where

$$\tilde{w}_k^+ = \frac{\gamma_k^+}{\tilde{\beta}_k^+}, \tag{A.17}$$

with the linear weights given by $\gamma_0^+ = 0.3$, $\gamma_1^+ = 0.6$, and $\gamma_2^+ = 0.1$. $\tilde{\beta}_k^+$ are the smoothness indicators given by

$$\tilde{\beta}_k^+ = \frac{\beta_k^+ + \varepsilon}{\beta_k^+ + \varepsilon + \tau_5^+}, \tag{A.18}$$

where β_k^+ is given by

$$\begin{aligned}
\beta_0^+ &= \frac{13}{12}\left(\xi_{j-1} - 2\xi_j + \xi_{j+1}\right)^2 + \frac{1}{4}\left(\xi_{j-1} - 4\xi_j + 3\xi_{j+1}\right)^2, \\
\beta_1^+ &= \frac{13}{12}\left(\xi_j - 2\xi_{j+1} + \xi_{j+2}\right)^2 + \frac{1}{4}\left(\xi_j - \xi_{j+2}\right)^2, \\
\beta_2^+ &= \frac{13}{12}\left(\xi_{j+1} - 2\xi_{j+2} + \xi_{j+3}\right)^2 + \frac{1}{4}\left(3\xi_{j+1} - 4\xi_{j+2} + \xi_{j+3}\right)^2,
\end{aligned} \tag{A.19}$$

and

$$\tau_5^+ = |\beta_0^+ - \beta_2^+|. \tag{A.20}$$